CAMBRIDGE
UNIVERSITY PRESS

RESEARCH ARTICLE

Structure design and kinematic performance of the deployable translational parallel tape-spring manipulator

Hu Liu [ORCID], Yawen Qin and Yi Yang

School of Mechatronic Engineering and Automation, Shanghai University, Shanghai, China
Corresponding author: Yi Yang; E-mail: yiyangshu@t.shu.edu.cn.

Abstract
A deployable manipulator has the characteristics of a small installation space and a large workspace, which has great application prospects in small unmanned platforms. Most existing deployable manipulators are designed based on rigid links, whose complexity and mass inevitably increase sharply with increasing numbers of rigid links and joints. Inspired by the remarkable properties of tape springs, this paper proposes novel deployable parallel tape-spring manipulators with low mass, simple mechanics, and a high deployed-to-folded ratio. First, a double *C*-shaped tape spring is presented to improve the stability of the structure. The combined fixed drive component (CFDC) and combined mobile drive component (CMDC) are designed. Then, novel 2-DOF and 3-DOF deployable translational parallel manipulators are proposed based on the CFDC and CMDC, and their degrees-of-freedom (DOFs), kinematics, and stability are analyzed. The coiled tape spring is regarded as an Archimedean spiral, which can significantly improve the accuracy of kinematic analysis. The correction coefficient of the Euler formula is obtained by comparison with simulation results and experimental results. Furthermore, the stability spaces of the 2-DOF and 3-DOF deployable parallel manipulators are given. Finally, a prototype is fabricated, and experiments are conducted to validate the proposed design and analysis.

1. Introduction

The deployable manipulator has the characteristics of small installation space and large workspace, which has great application prospects in small unmanned platforms such as satellites, unmanned aerial vehicles, and unmanned vehicles. Deployable mechanisms [1–8] can be folded into a small configuration for storage and expanded to a much larger structure for operation. Meanwhile, parallel manipulators such as DELTA [9], the Tricept robot [10], translational parallel manipulators [11–15], and spherical parallel manipulators [16–19] have parallel structures that improve the stiffness and accuracy of the manipulator [20, 21]. Deployable parallel manipulators, which combine the concepts of deployable mechanisms and parallel manipulators, have attracted increasing attention. Gonzalez et al. proposed a six-degree-of-freedom (6-DOF) parallel robot with a triple scissor extender for aircraft assembly [22]. A deployable manipulator with scissor linear joints that reduced the swept volume was designed by Chablat et al. [23]. Yang et al. designed certain parallel lower-mobility manipulators with dual scissor-like mechanisms (D-SLiMs) [24–27] and addressed the positioning error of this type of mechanism with a large span and low stiffness [28]. A novel deployable grasping manipulator for grasping large-scale objects was proposed by Li et al. [29].

The aforementioned deployable parallel manipulators were designed based on rigid links. However, with the increase in the number of rigid links and joints, the complexity and mass of the rigid deployable manipulator inevitably increase sharply, which greatly reduces the movement accuracy, stability, and reliability. Moreover, it is not easy to improve the deployed-to-folded ratio. This paper introduces the tape

spring into the design of deployable manipulators to overcome these limitations. The tape spring is a thin-walled open cylindrical structure with a natural transverse curvature and some remarkable properties [30, 31], such as being stiff before buckling but compliant thereafter and having a constant fold radius and moment after buckling [32, 33]. Deployable tape-spring manipulators have the advantages of low mass, simple mechanics, high folding efficiency, and no mechanical joints. Schmid designed deployable parallel manipulators with multiple tape springs [34]. Seriani et al. presented a 2-DOF manipulator that uses a pair of storable tubular extendible member actuators [35]. A chameleon-inspired shooting and rapidly retracting manipulator with a tape spring was developed by Lee et al. [36]. Yang et al. proposed two novel deployable parallel tape-spring manipulators [37]. The above deployable tape-spring manipulators have shortcomings in terms of stability and accuracy.

This paper proposes novel deployable parallel manipulators by taking advantage of the tape spring. A double *C*-shaped tape spring is presented to improve the stability of the structure. Inspired by the remarkable properties of tape springs, the combined fixed drive component (CFDC) and combined mobile drive component (CMDC) are designed. Based on the two kinds of drive components, 2-DOF and 3-DOF deployable translational parallel manipulators are designed, and their DOFs, kinematics, and stability are analyzed. The coiled tape spring is regarded as an Archimedean spiral in kinematic analysis, which can significantly improve the accuracy of kinematic analysis and facilitate kinematic control. The correction coefficient of the Euler formula is obtained by comparison with simulation results and experimental results. Furthermore, the boundary equations of the stability space of the manipulators are derived, and the stability spaces of the 2-DOF and 3-DOF parallel manipulators are given to avoid the instability phenomenon.

The remainder of this paper is organized as follows. In Section 2, the double C-shaped tape spring and two kinds of drive components are presented. In Sections 3 and 4, the structures, DOF analysis, and kinematics of the 2-DOF and 3-DOF deployable translational parallel tape-spring manipulators are presented. In Section 5, the stability of the manipulator is analyzed. The prototype is manufactured, and the experiment is conducted to validate the proposed design and analysis in Section 6. Finally, Section 7 presents the conclusions of the study.

2. Design of a double C-shaped tape spring and two drive components

2.1. Design of double C-shaped tape spring

The tape spring is a thin-walled open cylindrical structure that can achieve a deployable and folded state. To improve the stiffness and stability of the tape spring structure, two thin-walled open cylindrical structures are combined face-to-face to form a double C-shaped tape spring. They are tightly wrapped in a polyolefin tube by thermoforming, as shown in Fig. 1(a). This method could simplify the manufacturing process. Two open cylindrical structures are not fixed, reducing the creep effect of long-term accumulation. During the coiling process, the tight polyolefin tube can effectively reduce the tendency of the open cylindrical structure to buckle locally under pressure, improving the coiling efficiency. Fig. 1(b) shows the cross-section of the folded double *C*-shaped tape spring, which is flattened. The coiled double C-shaped tape spring is shown in Fig. 1(c), and the cross-sections of the deployable and folded segments correspond to Fig. 1(a) and (b), respectively. The double *C*-shaped tape spring structure can significantly improve the stiffness of the tape spring and the stability of the manipulator, which will be analyzed in Section 5.

2.2. Mobile drive component

The tape spring has unique properties. Fig. 2(a) shows that the straight segments of the tape spring can be stiff enough to withstand reasonable compressive loads before buckling, and the folded segments have zero transverse curvature. As shown in Fig. 2(b), the folded segment can slide along the tape spring if it is subjected to an external torque. Inspired by the above characteristics, we place the MDC on the
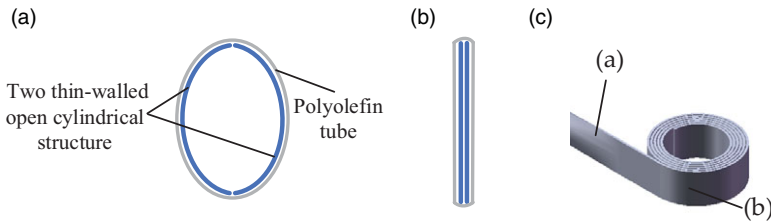
Figure 1. *Diagram of a double C-shaped tape spring. (a) Cross-section; (b) Cross-section after folding; (c) Coiled tape spring.*
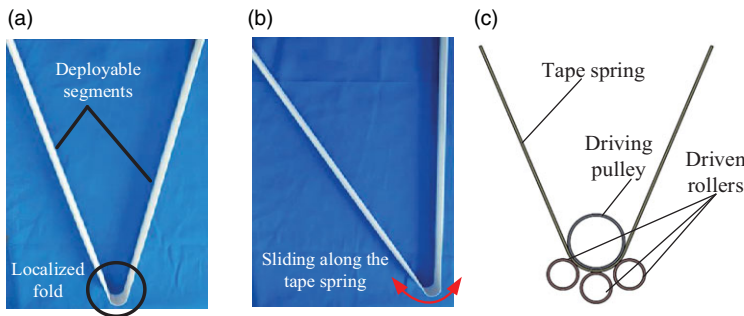

Figure 2. *Design principle of the MDC. (a) Localized folded configuration; (b) Folded segment of the tape spring sliding; (c) Schematic diagram of MDC.*
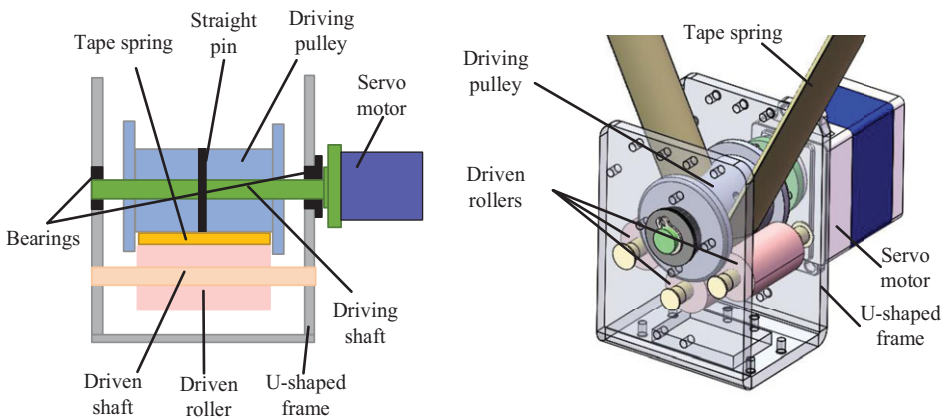

Figure 3. *The detailed structure of the mobile drive component.*

localized folded segment of the tape spring. The MDC has one driving pulley and three driven rollers, and the three driven rollers are paired under the driving pulley and located on the same arc, as shown in Fig. 2(c). The driving pulley and three driven rollers flatten the tape spring, reducing the folded segment's resistant torsion. As the driving pulley rotates, the MDC imposes an external torque on the fold, and the fold and the MDC can move along the tape spring.

The detailed structure of the MDC is shown in Fig. 3. The MDC mainly consists of a *U*-shaped frame, driving shaft, driving pulley, driven shaft, driven rollers, bearings, and a straight pin. When the driving pulley is actuated by the servo motor, the MDC and the localized fold can move along the tape spring.
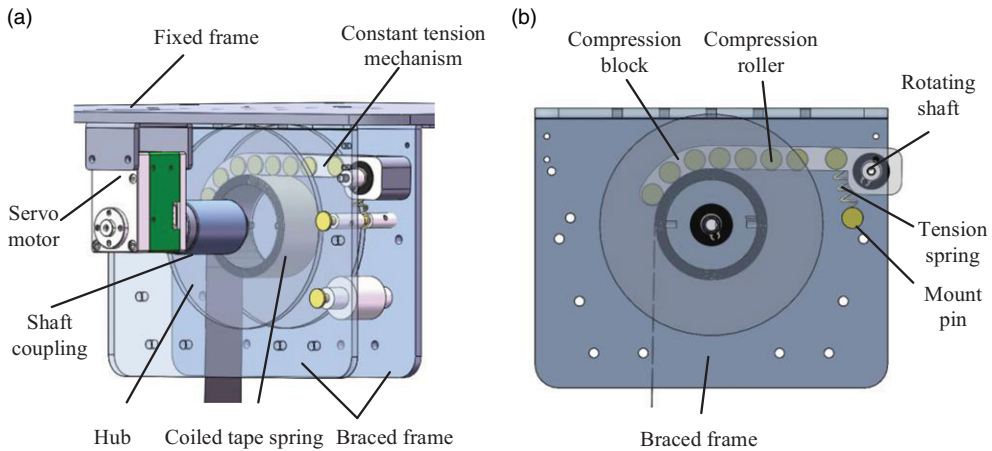
Figure 4. *Fixed drive component. (a) Structure; (b) Constant tension mechanism.*

2.3. Fixed drive component

The fixed drive component is designed to store the coiled tape spring and extend or retract the tape spring. The main parts of the FDC are a servo motor, a shaft coupling, a hub, a braced frame, a fixed frame, and a constant tension mechanism, as shown in Fig. 4(a). The servo motor and braced frame are mounted on the fixed frame. One end of the tape spring is fixed on the hub. The hub is connected to the servo motor by shaft coupling, and the tape spring can extend or retract by rotating the hub.

To flatten the tape spring and enhance motion reliability, a constant tension mechanism is designed to press the tape spring upon the hub. As shown in Fig. 4(b), the constant tension mechanism consists of a compression block, a rotating shaft, a tension spring, a mount pin, and a compression roller. While the tape spring is retracted or extended, the compression block presses the tape spring upon the hub, preventing it from expanding.

3. Structures and DOF analysis for two types of mechanisms

3.1. Structure and DOF analysis of a 2-DOF deployable parallel tape-spring manipulator

As shown in Fig. 5, the combined mobile drive component (CMDC) consists of two MDCs connected by a synchronous belt and a connecting rod. The connecting rod serves as the moving platform, and a gripper is mounted on it. Two MDCs can move synchronously by a servo motor. When the CMDC moves, the two MDCs may produce the same deviation angle with respect to the moving platform, but the moving platform does not produce the deviation angle relative to the horizontal axis. Therefore, the CMDC can solve the problem of the deviation angle of the MDC. Similarly, two FDCs are connected by a synchronous belt to form a combined fixed drive component.

Herein, a novel 2-DOF deployable parallel tape-spring manipulator is proposed based on CMDC and CFDC. As shown in Fig. 6, the double V-shaped 2-DOF deployable parallel manipulator consists of two tape springs, a CMDC, a CFDC, and two revolute joints. The CFDC is fixed on the aluminum frame, and the ends of the tape springs are hinged with the frame through the revolute joints. The CMDC located on the fold can move along the tape springs. The two FDCs are driven by a synchronous belt that allows the two V-shaped tape springs to simultaneously shorten or extend the same length. By controlling the CMDC and CFDC, the moving platform can translate in the plane.

Fig. 7 illustrates the schematic diagram of the mechanism. The mobile drive component can be considered as a 2-DOF kinematic pair, encompassing one translational mobility and one rotational mobility, as depicted in Fig. 7(a). The fixed drive component can be regarded as a 1-DOF kinematic pair with one translational mobility, as presented in Fig. 7(b).
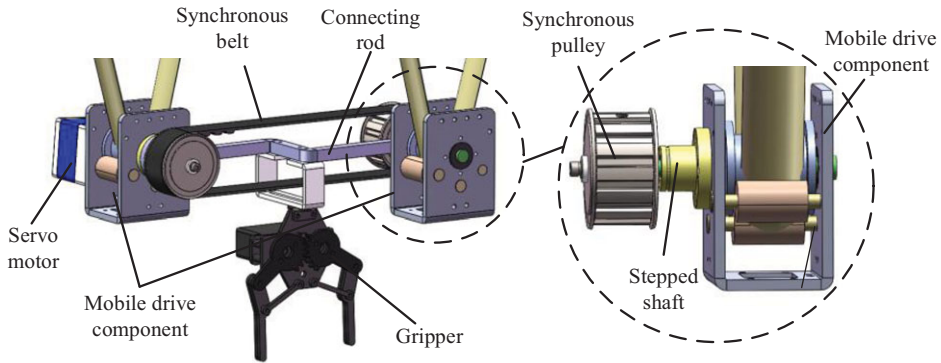
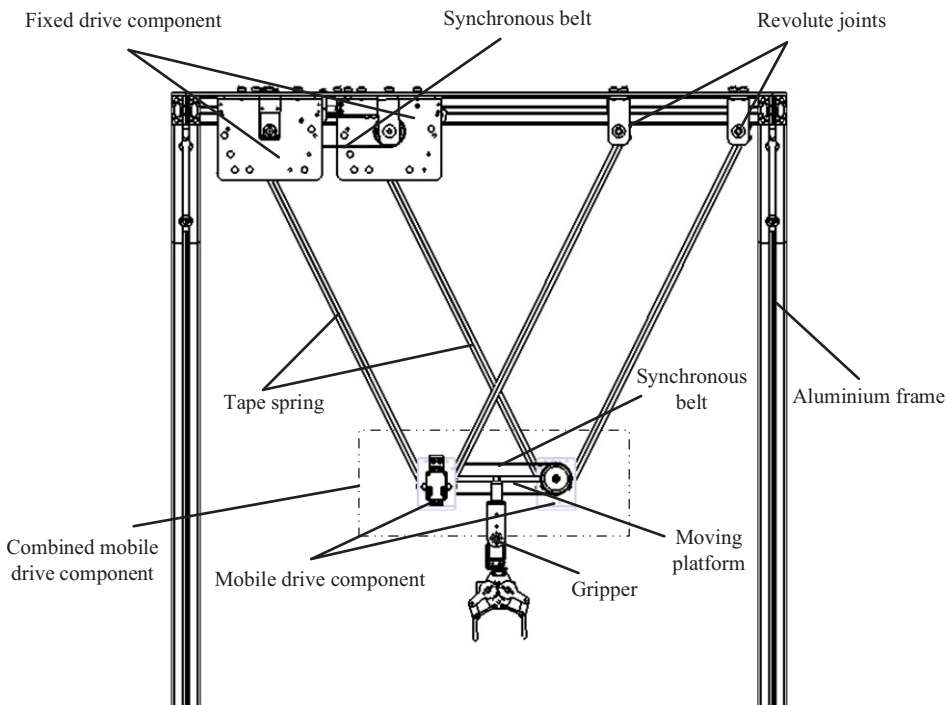**Figure 5.** *Combined mobile drive component.*

Figure 6. *2-DOF double V-shaped deployable parallel manipulator.*

To calculate the mobility of a mechanism, the Unified Modified G-K Criterion is given by relevant literature [38–40]

$$M = d(n - g - 1) + \sum_{i=1}^{g} f_i + v - \zeta \tag{1}$$

where M denotes the mobility of a mechanism, d is the order of a mechanism, n is the number of links including the frame, g is the number of kinematic joints, f_i is the number of freedoms of the ith joint, v is the number of redundant constraints except the number having been accounted in common constraints. ζ is the number of local freedoms.
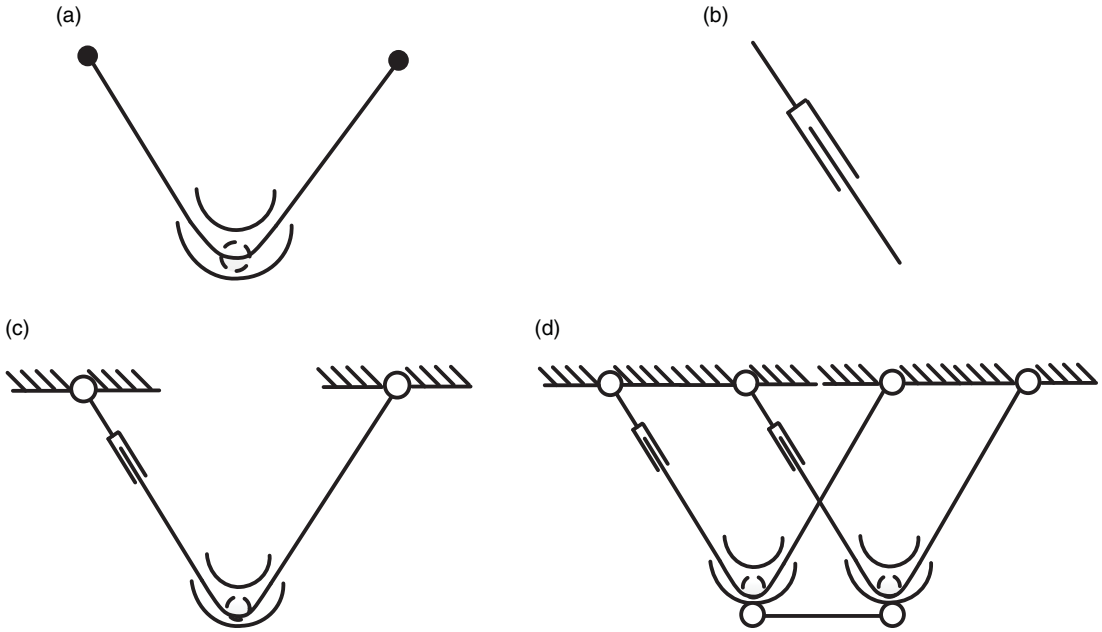
Figure 7. *Schematic diagram of the mechanism. (a). Mobile drive component, (b). Fixed drive component, (c). Single V-shaped configuration, (d). Double V-shaped configuration.*

The schematic diagram of the single V-shaped configuration is shown in Fig. 7(c). In this single V-shaped mechanism, n is 4, g is 4, $\sum_{i=1}^{4} f_i$ is 5. The mobility of this mechanism is

$$Ms = 3 \times (4 - 4 - 1) + 5 = 2 \tag{2}$$

We connect two V-shaped mechanisms in parallel, as shown in Fig. 7(d). The mobility of the double V-shaped mechanism is

$$Md = 3 \times (8 - 10 - 1) + 12 = 3 \tag{3}$$

By utilizing the Gr FC;bler's formula, we can initially determine the DOF of the mechanism. However, details regarding the DOF of the mechanism and how to increase constraints need further investigation through the screw theory.

The schematic diagram of the 2-DOF manipulator is shown in Fig. 8. D_1 and D_2 denote the FDCs, M_1 and M_1 denote the MDCs, and A_1 and A_2 denote the hinge joints which connect the end of the tape springs to the aluminum frame. D_1 and D_2, M_1 and M_2 are connected by synchronous belts to realize the synchronous motion. The lengths of D_1D_2, A_1A_2, and M_1M_2 are L_1, and D_1A_1 and D_2A_2 are L_2. The midpoint between D_1 and A_2 is set as the coordinate origin. The lengths of D_1M_1, M_1A_1, D_2M_2 and M_2A_2 are l_1, l_2, l_3 and l_4. Angles $\theta_1, \theta_2, \theta_3, \theta_4, \theta_5, \theta_6, \theta_{21}$, and θ_{41} are as shown in the figure. Therefore, the coordinates of each point are as follows: $D_1(x_{d1}, y_{d1}, 0), M_1(x_{m1}, y_{m1}, 0), D_2(x_{d1} + L1, y_{d1}, 0), M_2(x_{m1} + L1, y_{m1}, 0), A_1(x_{d1} + L2, y_{d1}, 0)$, and $A_2(x_{d1} + L1 + L2, y_{d1}, 0)$.

Then, the screw coordinates of the different joints can be determined. Limb D_1M_1 is used as an example, while other limbs are not listed.

$$
\begin{aligned}
\$_{D1} &= \begin{pmatrix} 0 & 0 & 1 & y_{d1} & -x_{d1} & 0 \end{pmatrix} \\
\$_{D1M1} &= \begin{pmatrix} 0 & 0 & 0 & x_{m1} - x_{d1} & y_{m1} - y_{d1} & 0 \end{pmatrix} \\
\$_{M1} &= \begin{pmatrix} 0 & 0 & 1 & y_{m1} & -x_{m1} & 0 \end{pmatrix}
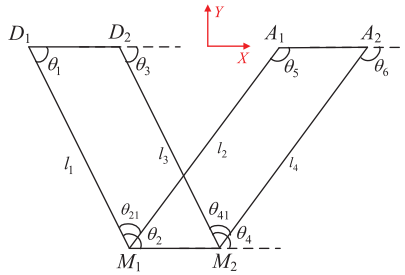\end{aligned}
\tag{4}
$$

Figure 8. *Schematic diagram of the 2-DOF manipulator.*

Specifically, selecting $D_1\widehat{M_1M_2}D_2$, $D_1\widehat{M_1}A_1$, and $D_2\widehat{M_2}A_2$, their screw equations are as follows:

$$\$_{D1}\dot{\theta}_1 + \$_{D1M1}\dot{l}_1 + \$_{M1}\dot{\theta}_2 = \$_{D2}\dot{\theta}_3 + \$_{D2M2}\dot{l}_3 + \$_{M2}\dot{\theta}_4$$
$$\$_{D1}\dot{\theta}_1 + \$_{D1M1}\dot{l}_1 + \$_{M1}\dot{\theta}_{21} = \$_{A1}\dot{\theta}_5 + \$_{A1M1}\dot{l}_2 \qquad (5)$$
$$\$_{D2}\dot{\theta}_3 + \$_{D2M2}\dot{l}_3 + \$_{M2}\dot{\theta}_{41} = \$_{A2}\dot{\theta}_6 + \$_{A2M2}\dot{l}_4$$

These equations can be formulated into the matrix,

$$
\begin{bmatrix}
\$_{D1} & \$_{M1} & -\$_{D2} & -\$_{M2} & 0 & 0 & 0 & 0 & \$_{D1M1} & 0 & -\$_{D2M2} & 0 \\
\$_{D1} & 0 & 0 & 0 & -\$_{A1} & 0 & \$_{M1} & 0 & \$_{D1M1} & -\$_{A1M1} & 0 & 0 \\
0 & 0 & \$_{D2} & 0 & 0 & -\$_{A2} & 0 & \$_{M2} & 0 & 0 & \$_{D2M2} & -\$_{A2M2}
\end{bmatrix}
\begin{bmatrix}
\dot{\theta}_1 \\ \dot{\theta}_2 \\ \dot{\theta}_3 \\ \dot{\theta}_4 \\ \dot{\theta}_5 \\ \dot{\theta}_6 \\ \dot{\theta}_{21} \\ \dot{\theta}_{41} \\ \dot{l}_1 \\ \dot{l}_2 \\ \dot{l}_3 \\ \dot{l}_4
\end{bmatrix} = 0
$$

$$(6)$$

where the coefficient matrix is

$$
Q = \begin{bmatrix}
\$_{D1} & \$_{M1} & -\$_{D2} & -\$_{M2} & 0 & 0 & 0 & 0 & \$_{D1M1} & 0 & -\$_{D2M2} & 0 \\
\$_{D1} & 0 & 0 & 0 & -\$_{A1} & 0 & \$_{M1} & 0 & \$_{D1M1} & -\$_{A1M1} & 0 & 0 \\
0 & 0 & \$_{D2} & 0 & 0 & -\$_{A2} & 0 & \$_{M2} & 0 & 0 & \$_{D2M2} & -\$_{A2M2}
\end{bmatrix}
$$

$$(7)$$

Determining the null space vectors of the coefficient matrix Q,

$$P = null(Q) \qquad (8)$$

This yields a three-column vector, indicating that the mechanism has 3 DOFs namely two translations and one rotation. To design a 2-DOF translational mechanism, it is necessary to maintain the parallelogram configuration, that is, $l_1 = l_3$ and $l_2 = l_4$. To satisfy these conditions, we introduce synchronous pulley constraints between M_1 and D_2, as well as between M_1 and M_2. Then, $\dot{l}_1 = \dot{l}_3$ and $\dot{l}_2 = \dot{l}_4$.
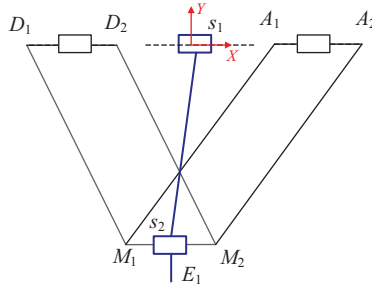
Figure 9. *Schematic diagram of the mechanism consisting of two 2-DOF manipulators.*

Therefore, the coefficient matrix is augmented by adding two rows for the constraints.

$$
Q = \begin{bmatrix}
\$_{D1} & \$_{M1} & -\$_{D2} & -\$_{M2} & 0 & 0 & 0 & 0 & \$_{D1M1} & 0 & -\$_{D2M2} & 0 \\
\$_{D1} & 0 & 0 & 0 & -\$_{A1} & 0 & \$_{M1} & 0 & \$_{D1M1} & -\$_{A1M1} & 0 & 0 \\
0 & 0 & \$_{D2} & 0 & 0 & -\$_{A2} & 0 & \$_{M2} & 0 & 0 & \$_{D2M2} & -\$_{A2M2} \\
0 & 0 & 0 & 0 & 0 & 0 & 0 & 0 & 1 & 0 & -1 & 0 \\
0 & 0 & 0 & 0 & 0 & 0 & 0 & 0 & 0 & 1 & 0 & -1
\end{bmatrix}
\tag{9}
$$

The null space vector of the coefficient matrix Q is two columns, indicating that the mechanism has 2 DOFs. We can select $\dot{l}_1$ and $\dot{l}_2$ as the two driving inputs. Substituting the null space vectors of the coefficient matrix Q into the expression $\$_{D1}\dot{\theta}_1 + \$_{D1M1}\dot{l}_1 + \$_{M1}\dot{\theta}_{21}$, two motion screws for the moving platform B_1B_2 can be obtained:

$$
\$_{M1M2} = \begin{bmatrix} 0 & 0 & 0 & 1 & 0 & 0 \\ 0 & 0 & 0 & 0 & 1 & 0 \end{bmatrix}
\tag{10}
$$

3.2. Structure and DOF analysis of a 3-DOF deployable parallel tape-spring manipulator

To further propose a 3-DOF deployable parallel tape-spring manipulator, we consider the 2-DOF manipulator as a sub-chain. As shown in Fig. 9, with the addition of a revolute joint based on the 2-DOF manipulator, the sub-chain can be equivalently represented by the blue lines.

The screw vectors for the endpoint of the equivalent sub-chain are:

$$
\$_{E1} \begin{cases}
\$_1 = \begin{pmatrix} 1 & 0 & 0 & 0 & 0 & -y_d \end{pmatrix} \\
\$_{M1M2} = \begin{pmatrix} 0 & 0 & 0 & 1 & 0 & 0 \\ 0 & 0 & 0 & 0 & 1 & 0 \end{pmatrix} \\
\$_2 = \begin{pmatrix} 1 & 0 & 0 & 0 & 0 & -y_m \end{pmatrix}
\end{cases}
\tag{11}
$$

The corresponding constraint screw is derived as follows:

$$
\$_{E1}^r = \begin{pmatrix} 0 & 0 & 0 & 0 & 1 & 0 \\ 0 & 0 & 0 & 0 & 0 & 1 \end{pmatrix}
\tag{12}
$$

When the above sub-chain is rotated by 90 degrees, the corresponding constraint screw for the endpoint of the sub-chain becomes:

$$
\$_{E2}^r = \begin{pmatrix} 0 & 0 & 0 & 1 & 0 & 0 \\ 0 & 0 & 0 & 0 & 1 & 0 \end{pmatrix}
\tag{13}
$$

The constraint screw of the mechanism constructed by the two sub-chains is

$$\$_{\mathrm{E}}^{r} = \begin{cases} \$_{\mathrm{E1}}^{r} \\ \$_{\mathrm{E2}}^{r} \end{cases} \tag{14}$$

Consequently, the DOF of the composite mechanism is

$$\$_{\mathrm{E}} = \begin{bmatrix} 0 & 0 & 0 & 1 & 0 & 0 \\ 0 & 0 & 0 & 0 & 1 & 0 \\ 0 & 0 & 0 & 0 & 0 & 1 \end{bmatrix} \tag{15}$$

Therefore, the composite mechanism has three translational mobilities. It is evident that if the end-points of the two sub-chains are rigidly connected, the moving platform of the parallel tape-spring mechanism exhibits three translational DOFs. In this context, each sub-chain contributes two input DOFs, denoted as $\dot{l}_1$ and $\dot{l}_2$. Therefore, the composite parallel mechanism has four input DOFs and three output DOFs.

To eliminate redundancy in the composite mechanism, one potential solution is to retain only one input DOF in one of the sub-chains. However, for the tape-spring mechanism, retaining only one input cannot guarantee the expected motion. This is due to the lower stiffness of tape springs compared to traditional rigid links. When the tape spring is significantly extended, ensuring effective force transmission becomes challenging. For instance, if the tape spring is subjected to substantial pressure, it might undergo buckling, resulting in the failure of the motion transmission. Therefore, we choose to preserve four input DOFs, while the output DOF is 3. However, there is another issue that needs to be considered. To achieve coordinated motion, these four input DOFs must maintain interdependent relationships. The mismatched motion may result in mechanical jamming or deformation, posing significant challenges for control.

To enhance the feasibility of the manipulator, when the moving platforms of two sub-chains are connected, a practical approach involves enabling relative vertical movement between these two moving platforms. This configuration translates the four inputs into four outputs, with one of the outputs representing the relative platform movement. In this way, even if there is a control deviation during motion, it may result in positional errors, but it will not lead to jamming or deformation. This design serves to enhance the practicality of the mechanism.

Overall, the 3-DOF parallel tape-spring manipulator is proposed as shown in Fig. 10. The distance between the center of the synchronous belt is L_1, and the distance between the FDC and the revolute joint is L_2. When $L_2 < L_1$, the double V-shaped parallel manipulator can evolve into the W-shaped parallel manipulator. Two W-shaped parallel manipulators are distributed vertically to form a 3-DOF translational manipulator. The 3-DOF manipulator is actuated by four servo motors, so it is a redundant manipulator. The 3-DOF manipulator mainly includes two 2-DOF W-shaped parallel manipulators, connections, rods, T-shaped connections, and moving rods. The manipulator is mounted on the aluminum frame. The T-shaped connection is fixed on the aluminum frame. Two bases are hinged to the T-shaped connections so that the moving platform is always parallel to the ground during the movement. The connections are hinged to the rods, and the moving rod is fixed on the upper connection, while the lower connection can translate along the moving rod. Relative motion can occur between two W-shaped parallel manipulators, reducing unstable movement caused by over-coupling. The 3-DOF tape-spring manipulator can realize space operation and is easy to control.

4. Kinematics of 2-DOF and 3-DOF deployable parallel tape-spring manipulators

4.1. Kinematic analysis of a 2-DOF deployable parallel tape-spring manipulator

The kinematic model of the 2-DOF deployable parallel tape-spring manipulator is shown in Fig. 11. D_1, D_2, M_1, and M_2 are connected by synchronous belts to realize synchronous motion. The lengths of D_1D_2, A_1A_2, and M_1M_2 are L_1, and D_1A_1 and D_2A_2 are L_2. Points D, M, and A are the midpoints of
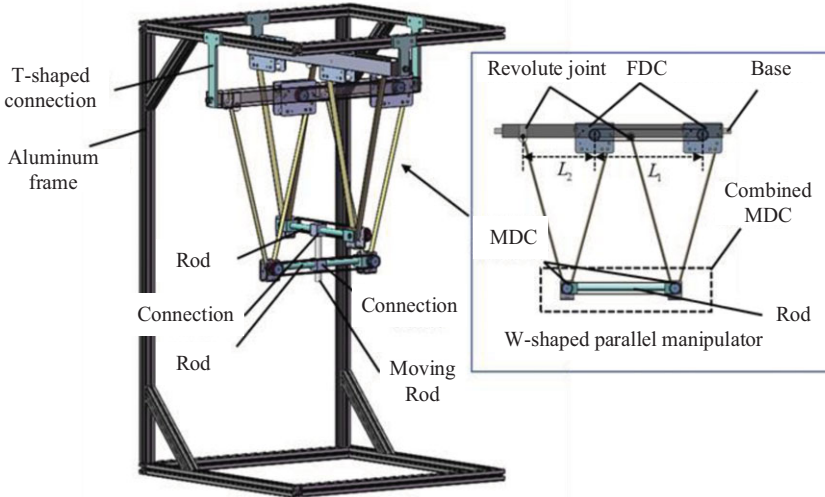
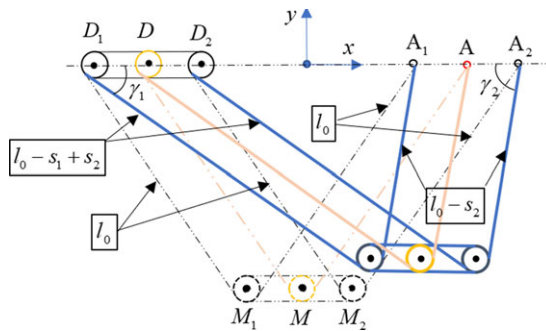**Figure 10.** *Detailed structure of the 3-DOF deployable tape-spring manipulator.*

Figure 11. *Kinematic model of the 2-DOF deployable parallel tape-spring manipulator.*

D_1D_2, M_1M_2, and A_1A_2, respectively. The midpoint between D_1 and A_2 is set as the coordinate origin. To simplify the kinematic model, the impact of the pulley radius on the positions of M_1 and M_2 is not considered. The initial lengths of the tape spring between D_1 and M_1, A_1 and M_1, D_2 and M_2, and A_2 and M_2 are all l_0. We assume that s_1 is the change in the overall length of the tape spring caused by the FDC D_1, that is, the length of the tape spring extending or shortening by rotating the hub. s_2 denotes the tape spring length variation between A_1 and M_1 caused by the MDC M_1. When D_1 rotates in a clockwise direction, s_1 is defined as positive. Likewise, when M_1 rotates in a clockwise direction, s_2 is defined as positive. The lengths of D_1M_1 and D_2M_2 are both $l_1 = l_0 - s_1 + s_2$, and M_1A_1 and M_2A_2 are $l_2 = l_0 - s_2$.

According to geometrical relationships, the coordinates of midpoint M of M_1M_2 are

$$
\begin{cases}
x = \dfrac{(2s_2 - s_1)(2l_0 - s_1)}{2L_2} \\
y = -\sqrt{(l_0 + s_2 - s_1)^2 - (x_0 + L_2/2)^2}
\end{cases}
\tag{16}
$$

According to Eq. (16), s_1 and s_2 can be expressed by x and y, respectively,

$$
\begin{cases}
s_1 = 2l_0 - \sqrt{(x + L_2/2)^2 + y^2} - \sqrt{(x - L_2/2)^2 + y^2} \\
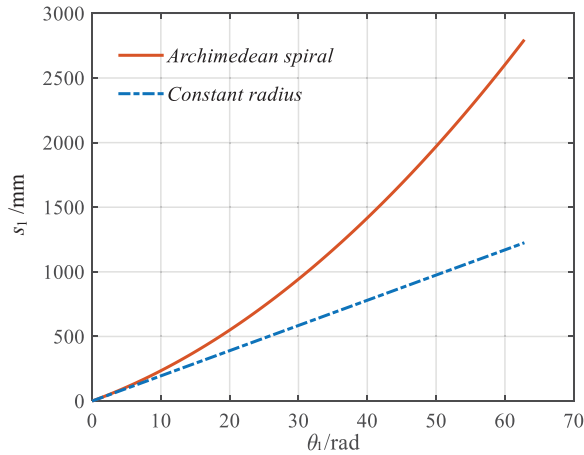s_2 = l_0 - \sqrt{(x - L_2/2)^2 + y^2}
\end{cases}
\tag{17}
$$

Figure 12. *The relationship between s_1 and the rotation angles of FDC θ_1 in two cases.*

Equation. (16) and (17) are the forward and inverse kinematic equations, respectively. Furthermore, s_1 and s_2 are analyzed as follows.

As the layer of the coiled tape spring increases, the radius of D_1 will increase. Therefore, the radius of D_1 is not constant. Herein, the coiled tape spring can be regarded as the Archimedes spiral. The radius of D_1 can be expressed as

$$r_1 = a + b\theta_1 \tag{18}$$

where a is the initial radius of the spiral, b is the rate of increase of the spiral, and θ_1 is the rotation angle of D_1. The arc length of the spiral is

$$L = \int \sqrt{r_1^2 + \left(\frac{dr_1}{d\theta_1}\right)^2} \, d\theta_1 \tag{19}$$

Therefore, we have

$$L(\theta_1) = \frac{b^2\theta_1 + ab}{2b^2} \sqrt{a^2 + b^2 + 2ab\theta_1 + b^2\theta_1^2} + \frac{b}{2} \operatorname{arcsinh}\left(\frac{b\theta_1 + a}{b}\right) + C \tag{20}$$

Herein, we assume that the initial angle of D_1 is 0. The tape spring length variations caused by the rotation angle of FDC θ_1 are denoted as s_1 and can be expressed as

$$s_1 = L(\theta_1) - L(0) \tag{21}$$

Given the initial radius $a = 19.5$ mm and the rate of increase of the spiral $b = 5/2\pi$ mm/rad, the relationship between s_1 and the rotation angles of FDC θ_1 is shown in Fig. 12. In addition, we also give the result when the radius r_1 is assumed to be constant. When the FDC is rotated by 50 rad, s_1 is approximately 2000 mm, while s_1 is 1000 mm if the coiled tape spring is considered a constant radius. In other words, s_1 is twice as large as the result if the coiled tape spring is considered a constant radius, and the error increases as the FDC rotates. Therefore, considering the coiled tape spring as an Archimedean spiral can significantly improve the accuracy of kinematic analysis and facilitate kinematic control.

The radius of MDC is r_2, and θ_2 is the corresponding rotation angle. The tape spring length variation s_2 due to the rotation angles of the MDC θ_2 is

$$s_2 = r_2\theta_2 \tag{22}$$

Differentiating Eq. (21) and (22) with respect to time, we have

$$\dot{s}_1 = \dot{L} = \dot{\theta}_1 \sqrt{(a + b\theta_1)^2 + b^2}$$
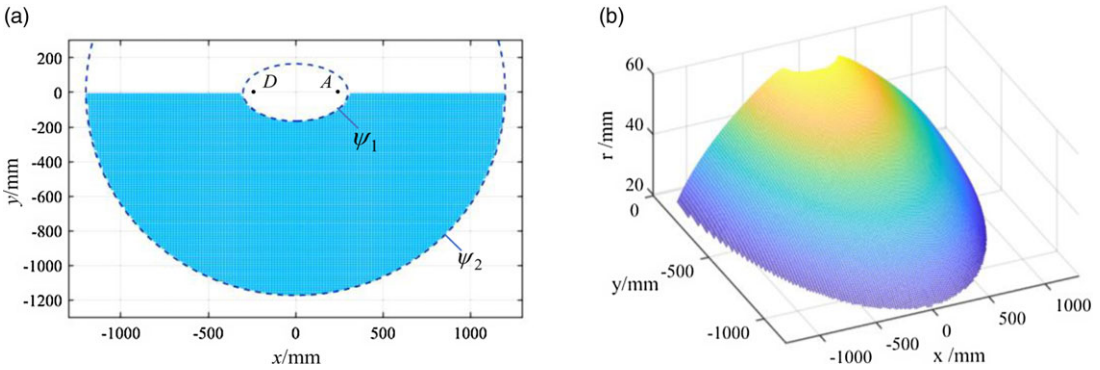$$\dot{s}_2 = r_2\dot{\theta}_2 \tag{23}$$

Figure 13. *(a) Workspace of the 2-DOF manipulator; (b) Variation of r_1 in the workspace.*

Based on the above formula, the workspace of the 2-DOF deployable parallel tape-spring manipulator can be given. When s_1 is invariable, the trajectory of M is an ellipse as s_2 changes, with the foci located at $D(-L_2/2, 0)$ and $A(L_2/2, 0)$. The focal length is $c = L_2/2$, the length of the major axis is $a = (2l_0 - s_1)/2$, and the length of the minor axis is $b = \sqrt{((2l_0 - s_1)/2)^2 - (L2/2)^2}$. Herein, assuming that the total length of the tape spring lies in the range $[\eta_{\min}, \eta_{\max}]$, the workspace can be regarded as the set of ellipses whose major axis is $a \in [\eta_{\min}/2, \eta_{\max}/2]$. Given the length $L_2 = 500$ mm, the maximum total length of the tape spring $\eta_{\max} = 2400$ mm, and its minimum total length $\eta_{\max} = 600$ mm, the workspace of the manipulator is shown in Fig. 13(a).

The boundary equations of the workspace ψ_1 and ψ_2 can be expressed as

$$
\begin{cases}
\psi_1: \dfrac{x^2}{(\eta_{\min}/2)^2} + \dfrac{y^2}{(\eta_{\min}/2)^2 - (L_2/2)^2} = 1 \\[4mm]
\psi_2: \dfrac{x^2}{(\eta_{\max}/2)^2} + \dfrac{y^2}{(\eta_{\max}/2)^2 - (L_2/2)^2} = 1
\end{cases}
\tag{24}
$$

As shown in Fig. 13(b), the radius of FDC r_1 varies in the working space. The radius r_1 lies in the range [19.5, 57] mm. The closer to the boundary ψ_1, the larger the radius. Conversely, the closer to the boundary ψ_2, the smaller the radius.

Differentiating Eq. (16) with respect to time, the velocity equations are

$$
\begin{bmatrix}
\dfrac{x + L_2/2}{\sqrt{(x + L_2/2)^2 + y^2}} & \dfrac{y}{\sqrt{(x + L_2/2)^2 + y^2}} \\[4mm]
\dfrac{x - L_2/2}{\sqrt{(x - L_2/2)^2 + y^2}} & \dfrac{y}{\sqrt{(x - L_2/2)^2 + y^2}}
\end{bmatrix}
\begin{bmatrix} \dot{x} \\ \dot{y} \end{bmatrix}
=
\begin{bmatrix} -1 & 1 \\ 0 & -1 \end{bmatrix}
\begin{bmatrix} \dot{s}_1 \\ \dot{s}_2 \end{bmatrix}
\tag{25}
$$

Equation (25) can be rewritten as

$$
J_K \begin{bmatrix} \dot{x} \\ \dot{y} \end{bmatrix} = \begin{bmatrix} \dot{s}_1 \\ \dot{s}_2 \end{bmatrix}
\tag{26}
$$

Let $l_1 = \sqrt{(x + L_2/2)^2 + y^2}$, and $l_2 = \sqrt{(x - L_2/2)^2 + y^2}$. The Jacobian matrix J_k is

$$
J_K =
\begin{bmatrix}
(L_2/2 - x)/l_2 - (L_2/2 + x)/l_1 & -y/l_1 - y/l_2 \\[2mm]
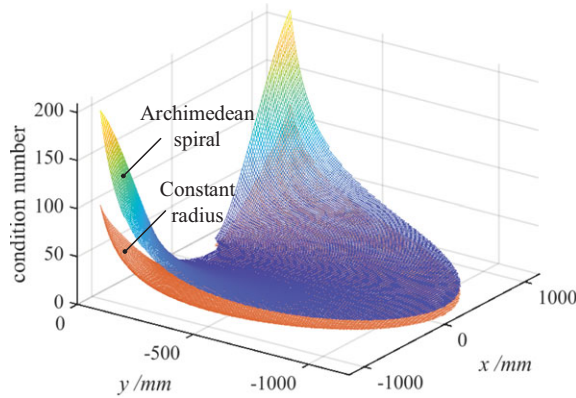(L_2/2 - x)/l_2 & -y/l_2
\end{bmatrix}
\tag{27}
$$

Figure 14. *Condition number of the Jacobian matrix under different conditions.*
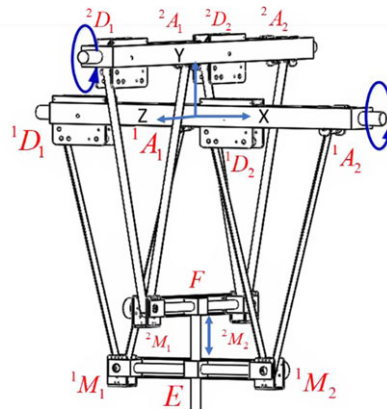

Figure 15. *Kinematic model of the 3-DOF deployable tape-spring manipulator.*

The determinant of J_k is

$$|J_K| = \frac{L_2 y}{l_1 l_2} \tag{28}$$

Equation (28) shows that the 2-DOF manipulator is singular when $y = 0$. Therefore, when the 2-DOF manipulator moves, the above condition should be avoided.

The condition numbers of Jacobian matrix J_k in the workspace are calculated to evaluate the kinematic performance of the manipulator, as shown in Fig. 14. The figure shows that the condition numbers become much larger as the moving platform approaches $y = 0$, indicating that the manipulator is singular when $y = 0$. In addition, we also give the result when r_1 is assumed to be constant. The condition number when the coiled tape spring is considered an Archimedean spiral is larger than that when the radius of the coiled tape spring is considered constant, and the difference is obvious. Therefore, it is necessary to consider the coiled tape spring as the Archimedes spiral in the kinematic analysis.

4.2. Kinematic analysis of the 3-DOF deployable tape-spring manipulator

The kinematic model of the 3-DOF deployable tape-spring manipulator is shown in Fig. 15. $^1A_1$, $^1A_2$, $^2A_1$, and $^2A_2$ denote revolute joints. $^1D_1$, $^1D_2$, $^2D_1$, and $^2D_2$ denote FDCs. $^1M_1$, $^1M_2$, $^2M_1$, and $^2M_2$ denote MDCs. E is the midpoint between $^1M_1$ and $^1M_2$, and F is the midpoint between $^2M_1$ and $^2M_2$. The coordinate origin O_1 is set in the middle between $^1D_1$ and $^1A_2$. The coordinates of O_2, which is the midpoint between $^2D_1$ and $^2A_2$, are $(0, h_0, 0)$. $^1D_1{}^1A_2$ can rotate about the X-axis, and $^2D_1{}^2A_2$ can rotate

about the Z-axis. $^1D_1$ and $^1D_2$, $^1M_1$ and $^1M_2$, $^2D_1$ and $^2D_2$, and $^2M_1$ and $^2M_2$ are connected by synchronous belts. The center distance of the synchronous belt is L_1, and the distance between the FDC and the revolute joint is L_2.

Herein, we assume that $^1s_1$ and $^2s_1$ are tape spring length variations caused by FDCs, and $^1s_2$ and $^2s_2$ are tape spring length variations caused by MDCs. The initial lengths of the tape spring between $^1D_1$ and $^1M_1$, $^1A_1$ and $^1M_1$, $^1D_2$ and $^1M_2$, $^1A_2$ and $^1M_2$, $^2D_1$ and $^2M_1$, $^2A_1$ and $^2M_1$, $^2D_2$ and $^2M_2$, and $^2A_2$ and $^2M_2$ are all l_0. The lengths of each tape spring segment can be expressed as

$$\begin{cases} l_{^1M_1{}^1A_1} = l_{^1M_2{}^1A_2} = l_0 + {}^1s_2 \\ l_{^1D_1{}^1M_1} = l_{^1D_2{}^1M_2} = l_0 - {}^1s_2 - {}^1s_1 \\ l_{^2M_1{}^2A_1} = l_{^2M_2{}^2A_2} = l_0 + {}^2s_2 \\ l_{^2D_1{}^2M_1} = l_{^2D_2{}^2M_2} = l_0 - {}^2s_2 - {}^2s_1 \end{cases} \tag{29}$$

We assume that the coordinate of the moving platform is $E(x, y, z)$. The lengths of $^1M_1{}^1A_1$ and $^1M_2{}^1A_2$ are l_1. The lengths of $^1D_1{}^1M_1$ and $^1D_2{}^1M_2$ are l_2. The lengths of $^2M_1{}^2A_1$ and $^2M_2{}^2A_2$ are l_3. The lengths of $^2D_1{}^2M_1$ and $^2D_2{}^2M_2$ are l_4. The following expressions are established from the geometric relation:

$$\begin{cases} \sqrt{\left(x - \dfrac{L_2}{2}\right)^2 + y^2 + z^2} = l_0 + {}^1s_2 = l_1 \\[2mm] \sqrt{\left(x + \dfrac{L_2}{2}\right)^2 + y^2 + z^2} = l_0 - {}^1s_2 - {}^1s_1 = l_2 \\[2mm] \sqrt{x^2 + (y + h_t - h_0)^2 + \left(z + \dfrac{L_2}{2}\right)^2} = l_0 + {}^2s_2 = l_3 \\[2mm] \sqrt{x^2 + (y + h_t - h_0)^2 + \left(z - \dfrac{L_2}{2}\right)^2} = l_0 - {}^2s_2 - {}^2s_1 = l_4 \end{cases} \tag{30}$$

Differentiating Eq. (30) with respect to time, the velocity equations are

$$\begin{bmatrix} \dfrac{(x - L_2/2)}{l_1} & y/l_1 & z/l_1 & 0 \\[2mm] \dfrac{(x + L_2/2)}{l_2} & y/l_2 & z/l_2 & 0 \\[2mm] x/l_3 & \dfrac{(y + h_t - h_0)}{l_3} & \dfrac{(z + L_2/2)}{l_3} & \dfrac{(y + h_t - h_0)}{l_3} \\[2mm] x/l_4 & \dfrac{(y + h_t - h_0)}{l_4} & \dfrac{(z - L_2/2)}{l_4} & \dfrac{(y + h_t - h_0)}{l_4} \end{bmatrix} \begin{bmatrix} \dot{x} \\ \dot{y} \\ \dot{z} \\ \dot{h}_t \end{bmatrix} = \begin{bmatrix} 1 & 0 & 0 & 0 \\ -1 & -1 & 0 & 0 \\ 0 & 0 & 1 & 0 \\ 0 & 0 & -1 & -1 \end{bmatrix} \begin{bmatrix} {}^1\dot{s}_2 \\ {}^1\dot{s}_1 \\ {}^2\dot{s}_2 \\ {}^2\dot{s}1 \end{bmatrix} \tag{31}$$

The Jacobian matrix J is

$$J = \begin{bmatrix} 1 & 0 & 0 & 0 \\ -1 & -1 & 0 & 0 \\ 0 & 0 & 1 & 0 \\ 0 & 0 & -1 & -1 \end{bmatrix}^{-1} \begin{bmatrix} \dfrac{(x - L_2/2)}{l_1} & y/l_1 & z/l_1 & 0 \\[2mm] \dfrac{(x + L_2/2)}{l_2} & y/l_2 & z/l_2 & 0 \\[2mm] x/l_3 & \dfrac{(y + h_t - h_0)}{l_3} & \dfrac{(z + L_2/2)}{l_3} & \dfrac{(y + h_t - h_0)}{l_3} \\[2mm] x/l_4 & \dfrac{(y + h_t - h_0)}{l_4} & \dfrac{(z - L_2/2)}{l_4} & \dfrac{(y + h_t - h_0)}{l_4} \end{bmatrix} \tag{32}$$
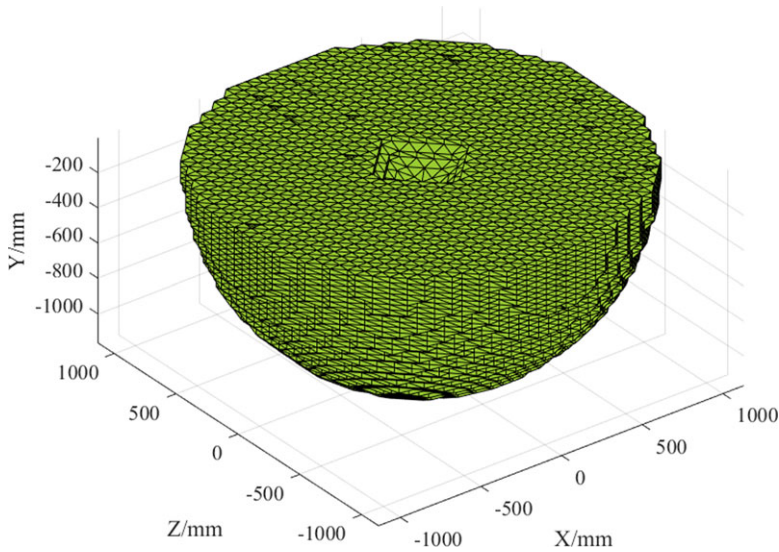
Figure 16. *Workspace of the 3-DOF deployable tape-spring manipulator.*

The determinant of the Jacobian matrix J is

$$|J| = \frac{L_2{}^2 y (h_t - h_0 + y)}{l_1 l_2 l_3 l_4} \tag{33}$$

Equation (33) shows that the 3-DOF manipulator is singular when $y = 0$ or $y = h_0 - h_t$. Therefore, when the 3-DOF manipulator moves, the above condition should be avoided.

It is assumed that the length changes of each straight segment caused by the driving component are dl_1, dl_2, dl_3, and dl_4, and the position changes of the moving platform are dx, dy, dz, and dh_t. The position of the moving platform and the variation in the length of the straight section of the tape spring can be expressed as follows:

$$
\begin{bmatrix}
\dfrac{(x - L_2/2)}{l_1} & y/l_1 & z/l_1 & 0 \\[2mm]
\dfrac{(x + L_2/2)}{l_2} & y/l_2 & z/l_2 & 0 \\[2mm]
x/l_3 & \dfrac{(y + h_t - h_0)}{l_3} & \dfrac{(z + L_2/2)}{l_3} & \dfrac{(y + h_t - h_0)}{l_3} \\[2mm]
x/l_4 & \dfrac{(y + h_t - h_0)}{l_4} & \dfrac{(z - L_2/2)}{l_4} & \dfrac{(y + h_t - h_0)}{l_4}
\end{bmatrix}
\begin{bmatrix} dx \\ dy \\ dz \\ dh_t \end{bmatrix}
=
\begin{bmatrix}
1 & 0 & 0 & 0 \\
0 & 1 & 0 & 0 \\
0 & 0 & 1 & 0 \\
0 & 0 & 0 & 1
\end{bmatrix}
\begin{bmatrix} dl_1 \\ dl_2 \\ dl_3 \\ dl_4 \end{bmatrix}
\tag{34}
$$

Substituting the length $L_2 = 350$ mm, $h_0 = h_t = 100$ mm, the maximum total length of the tape spring $\eta_{\max} = 2400$ mm, and its minimum total length $\eta_{\min} = 460$ mm into Eq. (34), the workspace of the 3-DOF manipulator is shown in Fig. 16.

5. Stability of the deployable parallel tape-spring manipulator

When the MDC moves along the tape spring, the part of the tape spring bears pressure, which means that the tape spring may buckle and disable the manipulator. The stability of the double C-shaped tape spring plays a crucial role in ensuring the stable motion of the manipulator. Hence, the stability of the manipulator is analyzed in this section.
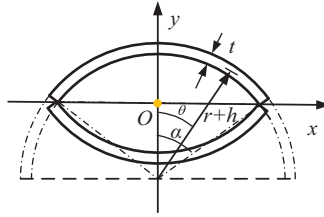
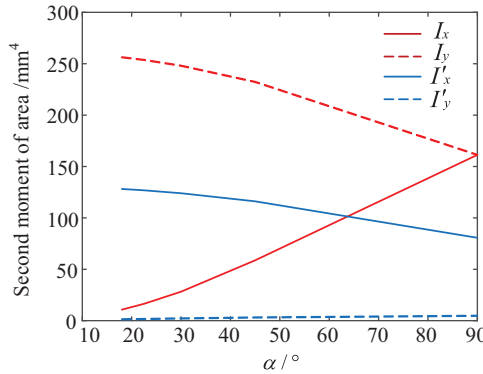**Figure 17.** *Cross-sectional geometry of the double C-shaped tape spring.*

Figure 18. *The second moment of the area corresponding to different α.*

5.1. Second moment of the area of the double C-shaped tape spring

To solve the stability workspace of the manipulator, it is necessary to analyze the buckling of the double C-shaped tape spring. The cross-sectional geometry of the double C-shaped tape spring is shown in Fig. 17, where r is the radius, t is the wall thickness, α is the angle of the arc edge to the vertical Y-axis, and $h \in [0, t]$ is the integration variable. Two thin-walled open cylindrical structures are tightly wrapped in a polyolefin tube, and the effect of the polyolefin tube is neglected. The second moment of the area of the double C-shaped tape spring is the sum of the two independent tape springs about the centroid O.

The cross-section of the double C-shaped tape spring is centrosymmetric, so the second moment of area I_x about the X-axis is

$$I_x = 4I_{x/4} = \left((r+t)^4 - r^4\right)\left(\frac{\sin 2\alpha}{4} + \frac{\alpha}{2}\right) - \frac{4(r+t)^3 r - 4r^4}{3}\sin 2\alpha - \left(4r^3 t + 2r^2 t^2\right)\alpha \cos^2 \alpha \quad (35)$$

Similarly, the second moment of area I_y about the Y-axis can be expressed as

$$I_y = 4I_{y/4} = \left((r+t)^4 - r^4\right)\left(\frac{\alpha}{2} - \frac{\sin 2\alpha}{4}\right) \quad (36)$$

The second moment of the area can be considered the upper limit for the bending stiffness and ultimate load. As shown in Fig. 18, the second moment of the area corresponding to different α values is investigated under a specific flattening width and wall thickness ($w = 25$ mm, $t = 0.1$ mm). With increasing α, I_x increases and I_y decreases gradually. The cross-section of the double C-shaped tape spring can be regarded as circular when $\alpha = 90°$, so I_x and I_y are equal. At this point, the double C-shaped tape spring has the best stability performance. In addition, the second moments of the area of the single tape spring about the X- and Y-axes are I'_x and I'_y. Under the same conditions, the second moment of the area of the double C-shaped tape spring is much larger than that of the single tape spring. Therefore, the manipulator we proposed adopts the double C-shaped tape spring, which can greatly improve the stability of the manipulator.
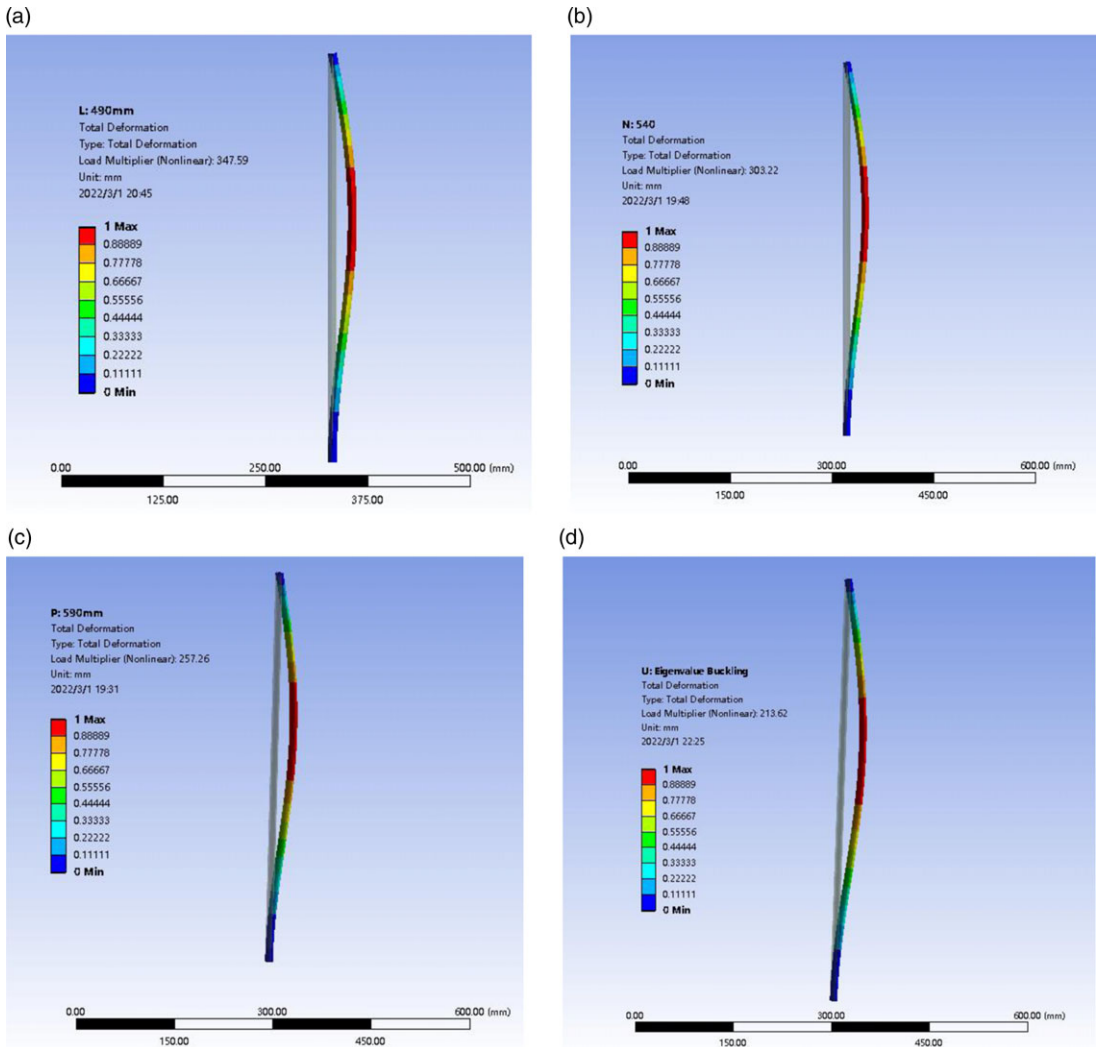
Figure 19. *Deformation diagram of a double C-shaped tape spring. (a) l = 490 mm; (b) l = 540 mm; (c) l = 590 mm; (d) l = 640 mm.*

5.2. Simulation analysis

Tape springs with lengths of 490 mm, 540 mm, 590 mm, and 640 mm are simulated by ANSYS. The elasticity and Poisson's ratio of the tape spring are set to $E = 1.31 \times 10^5 \text{N/mm}^2$ and 0.3, the elasticity and Poisson's ratio of the polyolefin tube are set to $E = 1070 \text{N/mm}^2$ and 0.41, and the actual load is set to 1. Fig. 19 shows the deformation diagram for the linear buckling of the tape springs. The simulation results of the tape springs with lengths of 490 mm, 540 mm, 590 mm, and 640 mm are 347 N, 303 N, 257 N, and 213 N, respectively.

5.3. Buckling experiment

The experimental configuration is shown in Fig. 20, mainly including a mechanical testing machine, fixture, and tape spring. The mechanical testing machine can obtain the load F and displacement of the rod end λ in real time. In the experiment, the moving speed of the loading mechanism is set as 5 mm/min. Buckling experiments are carried out on a tape spring with lengths of 490 mm, 540 mm, 590 mm, and
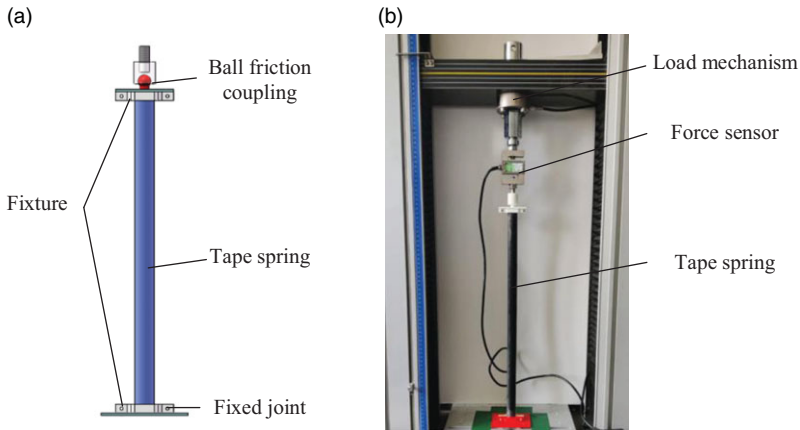
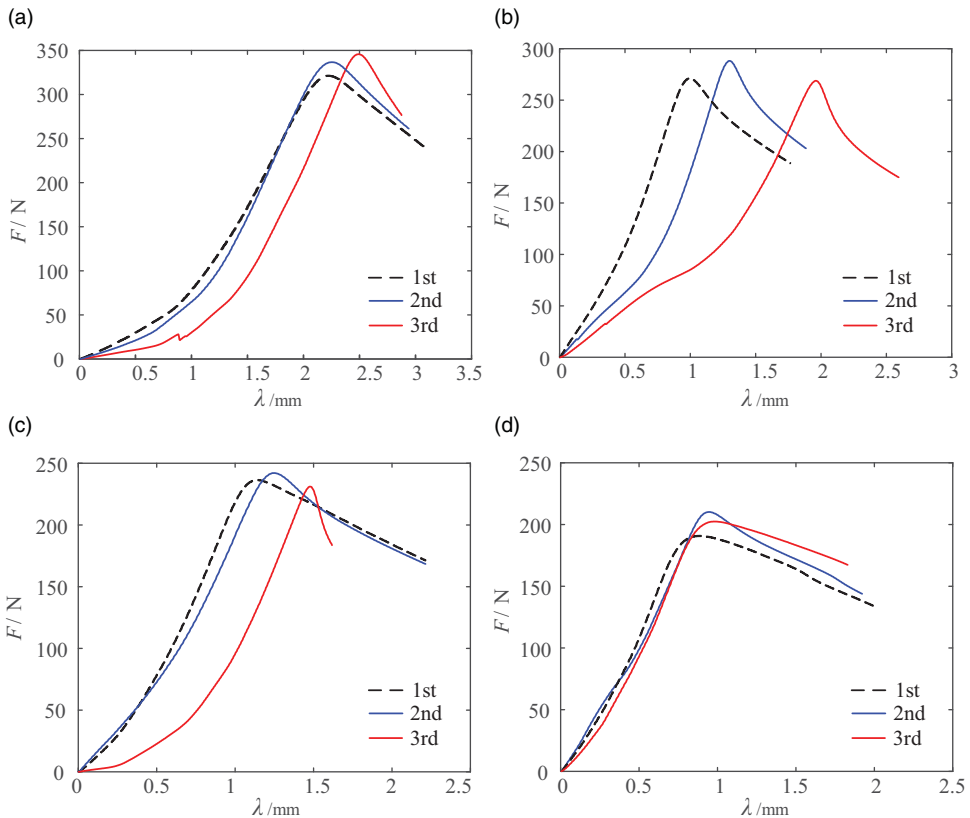**Figure 20.** *Configuration of the buckling experiment.*

Figure 21. *F-λcurves of double C-shaped tape springs with different lengths: (a) l = 490 mm; (b) l = 540 mm; (c) l = 590 mm; (d) l = 640 mm.*

640 mm. Experiments of each length are performed three times. *F*-λcurves of tape springs with different lengths are shown in Fig. 21.

For clarity, the experimental critical buckling loads of tape springs with different lengths are shown in Table I. For each length of tape spring, three experimental results and average values are given. As the length of the tape spring increases, the critical buckling loads gradually decrease.

Table I. *Critical buckling loads of the tape springs.*

Length/mm	Critical buckling load F/N			
	1st	2nd	3rd	average
490	345	321	336	334
540	268	270	288	275
590	231	236	242	236
640	192	202	210	201

Table II. *Comparison of critical loads for the tape spring obtained by three methods.*

Length (mm)	Theory (N)	Simulation (N)	Experiment (N)
490	384	347	334
540	316	303	275
590	265	257	236
640	225	213	201

5.4. Comparison of critical buckling load results obtained by the three methods

The buckling in axial compression of the tape spring is quite complex. In this section, we assume that the critical buckling case is Euler column buckling. The buckling load F is given by the Euler formula as

$$F = \frac{\pi^2 EI}{(Kl)^2} \tag{37}$$

where I is the second moment of the area of the tape spring, K is the column effective length factor, l is the length of the tape spring, and F is Euler's critical load. In the experiments and simulations, one end of the tape spring is fixed, and the other end is hinged. Substituting $K = 0.7$, $w = 25$mm, $t = 0.1$mm, $\alpha = 34°$, and $E = 1.31 \times 10^5$N/mm^2 into Eq. (37), the theoretical critical load is obtained.

The critical loads obtained from the theoretical calculation, simulation, and experiments are shown in Table II.

Table II shows that the theoretical, simulation, and experimental results are similar, and the theoretical and simulation values are higher than the experimental values. However, for practical application, the predicted value of the critical load of the tape spring should be below the experimental value to ensure stability and safety in the actual working process. To make the structure more reliable, the Euler formula is multiplied by a safety factor Φ to calculate the critical loads of the tape spring. Herein, according to the relevant literature [41–43] and experimental data, the safety factor is set as $\Phi = 0.85$. The modified Euler formula is

$$F = \frac{\zeta}{l^2} \tag{38}$$

where

$$\zeta = \Phi \frac{\pi^2 EI}{K^2} \tag{39}$$

To verify the accuracy of the modified Euler formula proposed in this paper, the calculated results of the modified Euler formula are plotted against the experimental results in Fig. 22. The theoretical calculation results using the modified Euler formula are smaller than the experimental values with small errors. This ensures the calculation accuracy as well as the stability and safety in the actual working process.
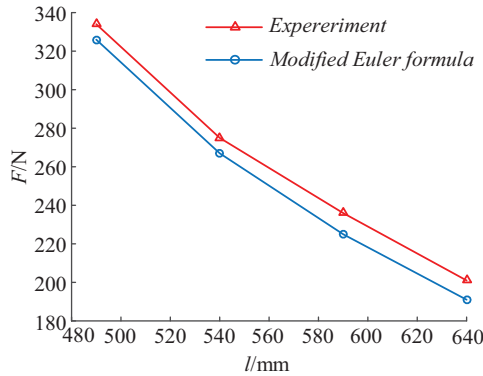
Figure 22. *Comparison between the modified Euler formula and experimental values.*

5.5. Stability spaces of 2-DOF and 3-DOF deployable parallel manipulators

The double V-shaped tape-spring manipulator can be simplified to a single *V*-shaped tape-spring manipulator *DMA*. The lengths of D_1M_1, D_2M_2, and *DM* are l_1, and the lengths of M_1A_1, M_2A_2, and *MA* are l_2. l_1 and l_2 can be expressed as

$$\begin{cases} l_1 = l_0 - s_1 + s_2 \\ l_2 = l_0 - s_2 \end{cases} \tag{40}$$

The *x*- and *y*-component forces upon the end-effector are denoted as f_x and f_y. Then, the compressions (tensions) f_{s1} and f_{s2} in *DM* and *MA* are

$$\begin{bmatrix} f_{s1} \\ f_{s2} \end{bmatrix} = \left(J_{Kl}^{\mathrm{T}} \right)^{-1} \begin{bmatrix} f_x \\ f_y \end{bmatrix} \tag{41}$$

Herein, we assume that f_y is always along the negative *Y*-axis. The Jacobian matrix J_K can be expressed as

$$J_K = \begin{bmatrix} (x + L_2/2)/l_1 & y/l_1 \\ (x - L_2/2)/l_2 & y/l_2 \end{bmatrix} \tag{42}$$

Then,

$$\left(J_K^{\mathrm{T}} \right)^{-1} = \begin{bmatrix} l_1/L_2 & (l_1(L_2 - 2x))/(2L_2y) \\ -l_2/L_2 & (l_2(L_2 + 2x))/(2L_2y) \end{bmatrix} \tag{43}$$

Substituting Eq. (43) into Eq. (41), the following equations can be obtained:

$$\begin{cases} f_{s1} = f_x l_1/L_2 + f_y(l_1(L_2 - 2x))/(2L_2y) \\ f_{s2} = -f_x l_2/L_2 + f_y(l_2(L_2 + 2x))/(2L_2y) \end{cases} \tag{44}$$

To maintain the stability of the manipulator, we require

$$\begin{cases} -f_{s1} \le \dfrac{2\zeta}{l_1^2} \ (f_{s1} < 0) \\[2mm] -f_{s2} \le \dfrac{2\zeta}{l_2^2} \ (f_{s2} < 0) \end{cases} \tag{45}$$

Γ_{s1} and Γ_{s2} denote the first and second boundaries of the stability space, respectively, which come from the first and second expressions in Eq. (45).
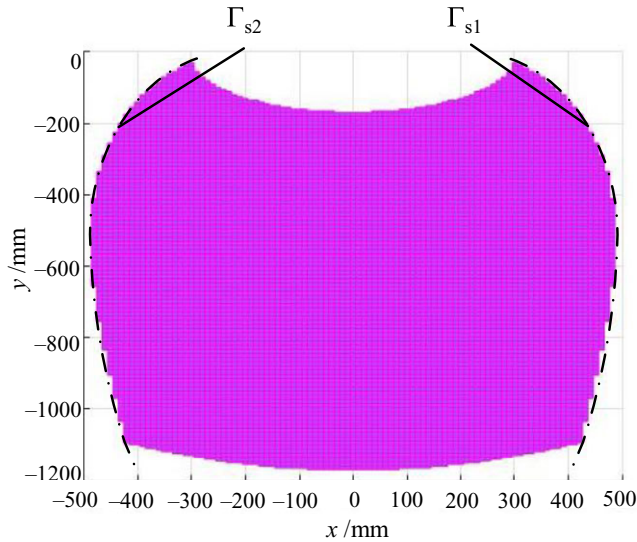
Figure 23. *Stability space of the 2-DOF manipulator.*

When calculating the stability space of the 2-DOF manipulator, only a vertical downward force on the end-effector is considered, that is, $f_y = -10$ N. The manipulator parameters are those given in Section 4. The corresponding stability space of the 2-DOF manipulator is shown in Fig. 23.

For the 3-DOF manipulator, the Jacobian matrix can be written as follows according to Eq. (34).

$$
J = \begin{bmatrix}
\dfrac{(x - L_2/2)}{l_1} & y/l_1 & z/l_1 & 0 \\[2mm]
\dfrac{(x + L_2/2)}{l_2} & y/l_2 & z/l_2 & 0 \\[2mm]
x/l_3 & \dfrac{(y + h_t - h_0)}{l_3} & \dfrac{(z + L_2/2)}{l_3} & \dfrac{(y + h_t - h_0)}{l_3} \\[2mm]
x/l_4 & \dfrac{(y + h_t - h_0)}{l_4} & \dfrac{(z - L_2/2)}{l_4} & \dfrac{(y + h_t - h_0)}{l_4}
\end{bmatrix}^{-1}
\begin{bmatrix}
1 & 0 & 0 & 0 \\
0 & 1 & 0 & 0 \\
0 & 0 & 1 & 0 \\
0 & 0 & 0 & 1
\end{bmatrix}
\tag{46}
$$

Assuming that the force on the end-effector of the 3-DOF manipulator is F, the relationship between F and the axial force N on the straight segment of each tape spring can be written as follows:

$$
N = J^T F \tag{47}
$$

Similarly, when calculating the stability space of the 3-DOF manipulator, only a vertical downward force on the end-effector is considered, that is, $F_y = -10$ N. When the axial force is less than the critical buckling load of the tape spring, it is regarded as the stability space of the manipulator, as shown in Fig. 24.

6. Prototype and experiments

The prototype of the 2-DOF deployable parallel tape-spring manipulator is manufactured to validate the previous design and analysis, as shown in Fig. 25. The manipulator is based on an aluminum frame. The FDCs and the revolute joints are installed on the top of the frame. The two tape springs are both 2400 mm long and 25 mm wide. Made of ABS material, the driving pulleys and driven rollers are 3D
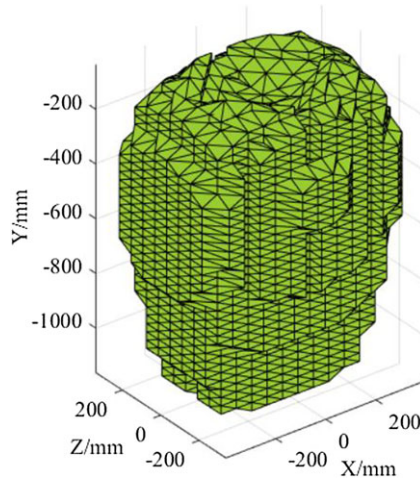
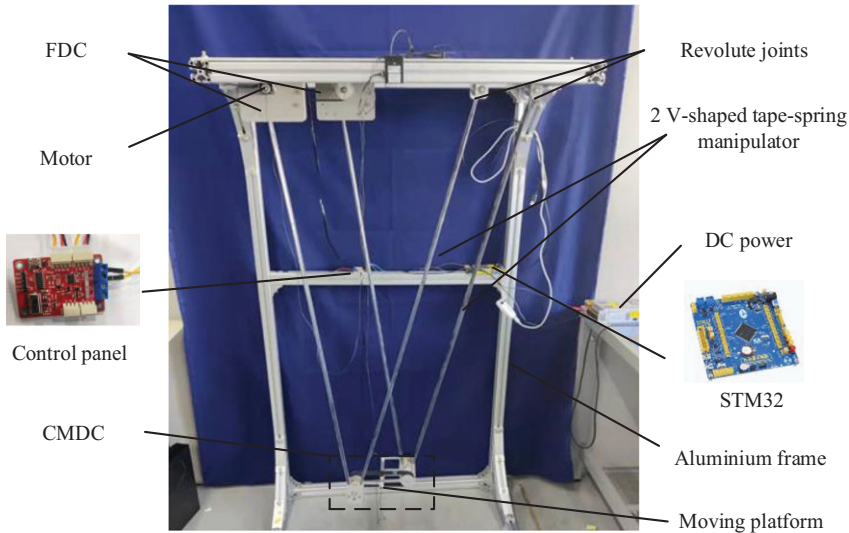**Figure 24.** *Stability space of the 3-DOF manipulator.*

Figure 25. *Prototype of the 2-DOF double V-shaped tape-spring manipulator.*

printed. The main diameter of the driving pulley is 25 mm, the diameter of the driven roller is 14 mm, and the width of the groove is 26 mm. The mass of the CMDC is 855 g, and the mass of the CFDC is 810 g. The manipulator control unit adopted one member of the STM32 F1 family of microcontrollers. It communicates with the driver board based on the TTL communication protocol. Then, the driver board transmits the control signal to the servo motor based on the TTL communication protocol. The servo motor in FMC is SM40BL by FEETECH, and the other one in MDC is SM30BL. By controlling the two motors in the FDC and MDC, the 2-DOF ultralight deployable parallel tape-spring manipulator can move smoothly along the X- and Y-axes.

To verify the stability space of the 2-DOF manipulator, a 1 kg weight is fixed on the end-effector platform. As shown in Fig. 26, we select four boundary positions to carry out the experiment. The experimental results validate the tape springs do not buckle in the stability space given in Section 5.5.

Fig. 27(a) illustrates the initial state of the experiment. The deployable manipulator is collapsed, and the object is placed at the bottom. The height between the gripper and the object is approximately
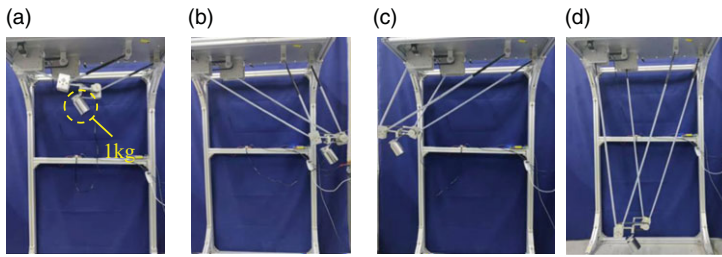
Figure 26. *Stability experiment at four boundary positions: (a) (0, −200); (b) (450, −500); (c) (−450, −500); (d) (−100, −1150).*
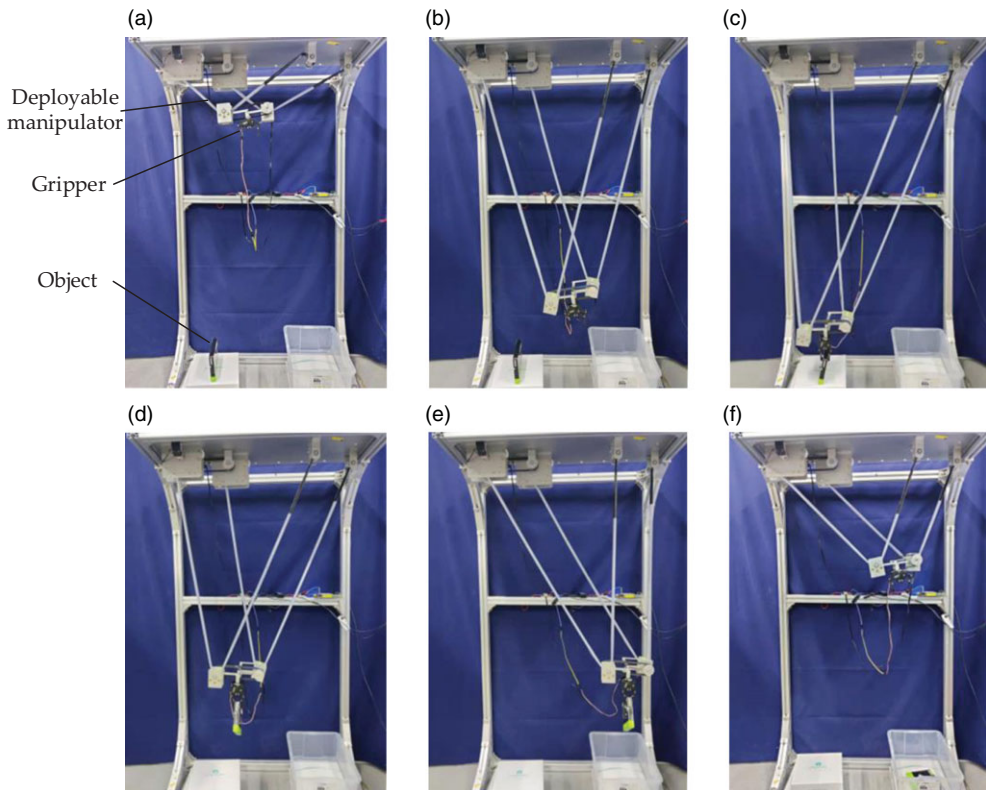

Figure 27. *Grasping experiment for the 2-DOF double V-shaped tape spring manipulator. (a) Initial state; (b) Deploying; (c) Grasping; (d) Moving to the right; (e) Releasing; (f) Retracting.*

800 mm. As shown in Fig. 27(b), the manipulator expands along the centerline by controlling two motors located in the FDC and MDC. Then, the manipulator moves to the left and grasps the object (Fig. 27(c)). Next, the manipulator moves above the right box and releases the object to the box, as shown in Fig. 27(d) and (e). Finally, the manipulator retracts to the initial state (Fig. 27(f)). In the experiment, the gripper could always be vertical to the ground and unaffected by the deviation angles of the MDC on each V-shaped tape spring. The motion of the manipulator is continuous and smooth. The experiment shows that the deployable parallel tape-spring manipulator has the advantages of a small installation space, a large workspace, and high stability.

7. Conclusions

This paper proposes novel deployable parallel manipulators by taking advantage of tape springs, such as variable stiffness, lightweight, and compact storage. The double *C*-shaped tape spring is presented, and the theoretical and experimental results show that it significantly increases the stability of the structure. Inspired by the remarkable properties of tape springs, the FDC and MDC are designed. Two MDCs are connected with a synchronous belt to form a combined mobile drive component, which can solve the problem of the deviation angle of the MDC. Based on the CFDC and CMDC, 2-DOF and 3-DOF deployable translational parallel manipulators are designed, and their DOFs, kinematics, and stability workspaces are analyzed. As the layer of the coiled tape spring increased, the radius r_1 increased. Hence, the coiled tape spring is regarded as an Archimedean spiral in kinematic analysis. When the FDC is rotated by 50 rad, the tape spring length variation s_1 is approximately 2000 mm, while s_1 is 1000 mm if r_1 is considered a constant radius. Meanwhile, the error increases as the FDC rotates. Therefore, considering the coiled tape spring as an Archimedean spiral can significantly improve the accuracy of kinematic analysis and facilitate kinematic control. The correction coefficient of the Euler formula is obtained by comparison with simulation results and experimental results. The modified Euler formula results are smaller than the experimental values with small errors. This ensures the accuracy of calculation as well as the stability and safety in the actual working process. Furthermore, the boundary equations of the stability space of the manipulators are derived, and the stability spaces of the 2-DOF and 3-DOF deployable parallel manipulators are given to avoid the instability phenomenon. Finally, a prototype is manufactured, and the experiment is conducted to verify the proposed design and analysis. The proposed manipulators have significant advantages in terms of lightweight, deployed-to-folded ratio, and stability and are suitable for unmanned platforms.

Further research can be conducted on the application of deployable parallel tape-spring manipulators mounted on small-scale platforms such as unmanned aerial vehicles and microsatellites.

Author contributions. Hu Liu conceived and designed the study. Hu Liu and Yawen Qin wrote the article. Yawen Qin conducted the experiments. Yi Yang supervised the research project and proofread the article.

Competing interests. The authors declare no competing interests exist.

Ethical approval. None.

References

[1] Z. You and S. Pellegrino, "Foldable bar structures," *Int J Solids Struct* **34**(15), 1825–1847 (1997). doi: 10.1016/S0020-7683(96)00125-4.

[2] G. Kiper, E. Söylemez and A. U. O. Kişisel, "A family of deployable polygons and polyhedra," *Mech Mach Theory* **43**(5), 627–640 (2008). doi: 10.1016/j.mechmachtheory.2007.04.011.

[3] X. Ding, Y. Yang and J. S. Dai, "Design and kinematic analysis of a novel prism deployable mechanism," *Mech Mach Theory* **63**, 35–49 (2013). doi: 10.1016/j.mechmachtheory.2013.01.001.

[4] S. Lyu, D. Zlatanov, M. Zoppi, X. Ding, G. S. Chirikjian and S. D. Guest, "Bundle folding type III bricard linkages," *Mech Mach Theory* **144**, 103663 (2020). doi: 10.1016/j.mechmachtheory.2019.103663.

[5] J. Wang and X. Kong, "Deployable mechanisms constructed by connecting orthogonal bricard linkages, 8R or 10R single-loop linkages using S joints," *Mech Mach Theory* **120**, 178–191 (2018). doi: 10.1016/j.mechmachtheory.2017.09.017.

[6] W. Zhang, S. Lu and X. Ding, "Recent development on innovation design of reconfigurable mechanisms in China," *Front Mech Eng* **14**(1), 15–20 (2019). doi: 10.1007/S11465-018-0517-7.

[7] Y. Chen, F. Yang and Z. You, "Transformation of polyhedrons," *Int J Solids Struct* **138**, 193–204 (2018). doi: 10.1016/j.ijsolstr.2018.01.012.

[8] R. Li, Y.-A. Yao and X. Ding, "A family of reconfigurable deployable polyhedral mechanisms based on semiregular and Johnson polyhedra," *Mech Mach Theory* **126**, 344–358 (2018). doi: 10.1016/J.MECHMACHTHEORY.2018.04.021.

[9] F. Pierrot, C. Reynaud and A. Fournier, "Delta: A simple and efficient parallel robot," *Robotica* **8**(2), 105–109 (1990). doi: 10.1017/S0263574700007669.

[10] B. Siciliano, "Tricept robot: Inverse kinematics, manipulability analysis and closed-loop direct kinematics algorithm," *Robotica* **17**(4), 437–445 (1999). doi: 10.1017/S0263574799001678.

[11] D. Chablat and P. Wenger, "Architecture optimization of a 3-DOF translational parallel mechanism for machining applications, the orthoglide," *IEEE Trans Robotic Autom* **19**(3), 403–410 (2003). doi: 10.1109/TRA.2003.810242.

[12] X.-J. Liu, J. I. Jeong and J. Kim, "A three translational DoFs parallel cube-manipulator," *Robotica* **21**(6), 645–653 (2003). doi: 10.1017/S0263574703005198.

[13] M. Carricato and V. Parenti-Castelli, "Kinematics of a family of translational parallel mechanisms with three 4-DOF legs and rotary actuators," *J Robot Syst* **20**(7), 373–389 (2003). doi: 10.1002/rob.10092.

[14] X. Kong and C. M. Gosselin, "Type synthesis of 3-DOF translational parallel manipulators based on screw theory," *J Mech Design* **126**(1), 83–92 (2004). doi: 10.1115/1.1637662.

[15] W. Yu, H. Wang and G. Chen, "Design and kinematic analysis of a 3-translational-DOF spatial parallel mechanism based on polyhedra," *Mech Mach Theory* **121**, 92–115 (2018). doi: 10.1016/j.mechmachtheory.2017.10.020.

[16] X. Kong and C. M. Gosselin, "Type synthesis of 3-DOF spherical parallel manipulators based on screw theory," *J Mech Design* **126**(1), 101–108 (2004). doi: 10.1115/1.1637655.

[17] R. Di Gregorio, "A new family of spherical parallel manipulators," *Robotica* **20**(4), 353–358 (2002). doi: 10.1017/S0263574702004174.

[18] D. Shi, W. Zhang, W. Zhang and X. Ding, "Assist-as-needed attitude control in three-dimensional space for robotic rehabilitation," *Mech Mach Theory* **154**, 104044 (2020). doi: 10.1016/j.mechmachtheory.2020.104044.

[19] Z. Wang, W. Zhang and X. Ding, "Design and analysis of a novel mechanism with a two-DOF remote centre of motion," *Mech Mach Theory* **153**, 103990 (2020). doi: 10.1016/j.mechmachtheory.2020.103990.

[20] K. Marlow, M. Isaksson, J. S. Dai and S. Nahavandi, "Motion/Force transmission analysis of parallel mechanisms with planar closed-loop subchains," *J Mech Design* **138**(6), 062302, 11 pages (2016). doi: 10.1115/1.4033338.

[21] Q. Meng, F. Xie, X.-J. Liu and Y. Takeda, "An evaluation approach for motion-force interaction performance of parallel manipulators with closed-loop passive limbs," *Mech Mach Theory* **149**, 103844 (2020). doi: 10.1016/j.mechmachtheory.2020.103844.

[22] D. J. Gonzalez and H. H. Asada, "Design and analysis of 6-DOF triple scissor extender robots with applications in aircraft assembly," *IEEE Robot Autom Lett* **2**(3), 1420–1427 (2017). doi: 10.1109/LRA.2017.2671366.

[23] D. Chablat, L. Rolland and R. Luc, "Design of mechanisms with scissor linear joints for swept volume reduction" (2016) 2–3.

[24] Y. Yang, Y. Tian, Y. Peng and H. Pu, "A novel 2-DOF planar translational mechanism composed by scissor-like elements," *Mech Sci* **8**(1), 179–193 (2017). doi: 10.5194/ms-8-179-2017.

[25] Y. Yang, Y. Peng, H. Pu, H. Chen, X. Ding, G. S. Chirikjian and S. Lyu, "Deployable parallel lower-mobility manipulators with scissor-like elements," *Mech Mach Theory* **135**, 226–250 (2019). doi: 10.1016/j.mechmachtheory.2019.01.013.

[26] Y. Yang, H. Liu, H. Zheng, Y. Peng and Y. Yu, "Two types of remote-center-of-motion deployable manipulators with dual scissor-like mechanisms," *Mech Mach Theory* **160**, 104274 (2021). doi: 10.1016/j.mechmachtheory.2021.104274.

[27] Y. Yang, L. Tang, H. Zheng, Y. Zhou, Y. Peng and S. Lyu, "Kinematic stability of a 2-DOF deployable translational parallel manipulator," *Mech Mach Theory* **160**, 104261 (2021). doi: 10.1016/j.mechmachtheory.2021.104261.

[28] H. Liu, Y. Yang, Y. Zhao, Y. Yang, Y. Peng, H. Pu and Y. Zhou, "Learning-based kinematic control of a deployable manipulator with long span and low stiffness," *IEEE/ASME Trans Mech* **29**(1), 742–753 (2024). doi: 10.1109/TMECH.2023.3296698.

[29] G. Li, H. Huang, H. Guo and B. Li, "Design, analysis and control of a novel deployable grasping manipulator," *Mech Mach Theory* **138**, 182–204 (2019). doi: 10.1016/j.mechmachtheory.2019.03.043.

[30] M. G. De Jong, W. W. P. J. Van De Sande and J. L. Herder, "Properties of twofold tape loops: The influence of the subtended angle," *J Mech Robot* **11**(2), 020912, 7 pages (2019). doi: 10.1115/1.4042641/472393.

[31] C. Vehar, S. Kota and R. Dennis, "Closed-Loop Tape Springs as Fully Compliant, Mechanisms -Preliminary Investigations," **In:** *Proceedings of the ASME Design Engineering Technical Conference and Computers and Information in Engineering Conference*, vol. 46954, (2004) pp. 1023–1032. doi: 10.1115/DETC2004-57403.

[32] C. R. Calladine, "The Theory of Thin Shell Structures 1888–1988," *Proceed Inst Mech Eng, Part A: Power Proc Eng* **202**(3), 141–149 (1988). doi: 10.1243/PIME_PROC_1988_202_020_02.

[33] K. A. Seffen and S. Pellegrino, "Deployment dynamics of tape springs," *Proceed Roy Soc London. A: Math Phys Eng Sci* **455**(1983), 1003–1048 (1999). doi: 10.1098/RSPA.1999.0347.

[34] S. Hochreiter and J. Schmidhuber, "Long short-term memory, neural comput," *Neu comp* **9**(8), 1735–1780 (1997). doi: 10.1162/neco.1997.9.8.1735.

[35] S. Seriani and P. Gallina, "A storable tubular extendible member (STEM) parallel robot: Modelization and evaluation," *Mech Mach Theory* **90**, 95–107 (2015). doi: 10.1016/j.mechmachtheory.2015.03.010.

[36] D.-J. Lee and G.-P. Jung, "Snatcher: A highly mobile chameleon-inspired shooting and rapidly retracting manipulator," *IEEE Robot Autom Lett* **5**(4), 6097–6104 (2020). doi: 10.1109/LRA.2020.3010744.

[37] Y. Yang, Y. Qin, Y. Tang, Y. Yang, Y. Peng and H. Pu, "Deployable closed-loop tape-spring manipulators with mobile drive components on localized folds," *Mech Mach Theory* **167**, 104553 (2022). doi: 10.1016/j.mechmachtheory.2021.104553.

[38] G. Gogu, "Chebychev-Grübler-Kutzbach's criterion for mobility calculation of multi-loop mechanisms revisited via theory of linear transformations," *European J Mech - A/Solids* **24**(3), 427–441 (2005). doi: 10.1016/J.EUROMECHSOL.2004.12.003.

[39] G. Gogu, "Mobility of mechanisms: A critical review, mech mach theory," *Mech Mach Theory* **40**(9), 1068–1097 (2005). doi: 10.1016/J.MECHMACHTHEORY.2004.12.014.

[40] J. S. Dai and J. R. Jones, "Mobility in metamorphic mechanisms of foldable/Erectable kinds," *J Mech Design* **121**(3), 375–382 (1999). doi: 10.1115/1.2829470.

[41] A. Zureick and D. Scott, "Short-term behavior and design of fiber-reinforced polymeric slender members under axial compression," *J Compos Constr* **1**(140), 140–149 (1997). doi: 10.1061/(ASCE)1090-0268(1997)1:.

[42] E. Dulácska and L. Kollár, "Buckling analysis of reticulated shells, http: //Dx. Doi. Org/10.1260/0266351001495134," *Int J Space Struc* **15**(3), 195–203 (2000). doi: 10.1260/0266351001495134.

[43] M. K. Lee, H. Lee, T. S. Lee and H. Jang, "Buckling sensitivity of a connecting rod to the shank sectional area reduction," *Mater Des* **31**(6), 2796–2803 (2010). doi: 10.1016/J.MATDES.2010.01.010.